Elastic wave manipulation by using a phase-controlling meta-layer

Xiaohui Shen, Chin-Teh Sun, Miles V. Barnhart, and Guoliang Huang

Citation: Journal of Applied Physics **123**, 091708 (2018);
View online: https://doi.org/10.1063/1.4996018
View Table of Contents: http://aip.scitation.org/toc/jap/123/9
Published by the American Institute of Physics

JOURNAL OF APPLIED PHYSICS **123**, 091708 (2018)

Elastic wave manipulation by using a phase-controlling meta-layer

Xiaohui Shen,[1,2] Chin-Teh Sun,[1] Miles V. Barnhart,[2] and Guoliang Huang[2,a)]
[1]*School of Aeronautics and Astronautics, Purdue University, West Lafayette, Indiana 47907, USA*
[2]*Department of Mechanical and Aerospace Engineering, University of Missouri, Columbia, Missouri 65211, USA*

(Received 13 July 2017; accepted 4 October 2017; published online 27 December 2017)

In this work, a high pass meta-layer for elastic waves is proposed. An elastic phase-controlling meta-layer is theoretically realized using parallel and periodically arranged metamaterial sections based on the generalized Snell's law. The elastic meta-layer is composed of periodically repeated supercells, in which the frequency dependent elastic properties of the metamaterial are used to control a phase gradient at the interface between the meta-layer and conventional medium. It is analytically and numerically demonstrated that with a normal incident longitudinal wave, the wave propagation characteristics can be directly manipulated by the periodic length of the meta-layer element at the sub-wavelength scale. It is found that propagation of the incident wave through the interface is dependent on whether the working wavelength is longer or shorter than the periodic length of the meta-layer element. Specifically, a mode conversion of the *P*-wave to an *SV*-wave is investigated as the incident wave passes through the meta-layer region. Since the most common and damaging elastic waves in civil and mechanical industries are in the low frequency region, the work in this paper has great potential in the seismic shielding, engine vibration isolation, and other highly dynamic fields. *Published by AIP Publishing.* https://doi.org/10.1063/1.4996018

I. INTRODUCTION

The concept of metamaterials was originated in the field of electromagnetics (EM) in 1968 when Veselago[1] postulated that if the electric permittivity and the magnetic permeability of a material were simultaneously negative, it would result in a left-handed medium.[2] This type of medium would produce abnormal phenomena such as reversal of the Doppler shift, Cherenkov radiation, and negative refraction.[3] However, as pointed out by Veselago, substances with a negative magnetic permeability were not available, and therefore, this novel idea did not get much attention at that time. Three decades later, Pendry realized the effective negative electric permittivity[4] and proposed a split ring resonator medium, which generated a negative permeability.[5] From then on, many researchers have started to enter the study of metamaterials.

Inspired by electromagnetic (EM) metamaterials, acoustic/elastic metamaterials have started to gain a great deal of attention over the last decade. Analogous to negative permittivity and permeability in EM metamaterials, researchers first focused on realizing acoustic metamaterials with man-made microstructures that exhibit negative effective mass and/or negative effective modulus, which were not found in natural materials. In 2000, Liu *et al.*[6] proposed the first man-made metamaterial using rubber-coated lead spheres to create a local resonance mechanism, which enabled the material to exhibit negative effective mass in certain frequency region. In 2006, Fang *et al.*[7] reported a new type of acoustic metamaterial with a negative effective modulus. This new acoustic metamaterial consisted of an array of subwavelength Helmholtz resonators that were demonstrated theoretically and experimentally to possess a dynamic effective modulus with negative values near the resonance frequency of the Helmholtz resonators. It can be concluded that these peculiar mechanical characteristics of metamaterials are originated from the frequency dependent resonance mechanism.

In recent years, the acoustic metasurface concept has gained a great deal of research attention.[8–13] An acoustic metasurface is a layer comprised of parallel, periodically arranged metamaterial sections. In contrast to the previous metamaterial designs, the characteristic feature of the metasurface is its subwavelength thickness. With this property, the acoustic metasurface represents an important advance in the miniaturization of acoustic devices.[8] Using decorated membrane resonators, Ma *et al.*[9] fabricated an impedance-matched surface that generated no reflections when impinged by an incident wave. Based on the generalized Snell's law of reflection,[13] Zhao *et al.*[10] established a framework for acoustic wave front manipulation through an inhomogeneous acoustic impedance. Mei and Wu[8] proposed a type of acoustic metasurface with periodically repeated supercells placed on a thin rigid plate, where each supercell could produce a constant wave phase delay. It was also numerically demonstrated that the normal incident wave could be reflected entirely when its wavelength is larger than the periodicity, but almost entirely transmitted when the wavelength is smaller than the periodicity. Zhu and Semperlotti[14] investigated geometrically tapered acoustic metasurface designs capable of guiding elastic waves in thin-walled structural elements both numerically and experimentally. Using the generalized Snell's law, it was demonstrated that the acoustic metasurface design possessed unique properties in the refraction of guided wave modes. In experimental testing, the locally resonant torus-like tapers were shown to allow for an accurate phase shift of incident waves, which altered the metasurface's refractive properties. Ma *et al.*[9] experimentally demonstrated an acoustic metasurface

[a)]Author to whom correspondence should be addressed: huangg@missouri.edu

capable achieving zero reflection of incident acoustic waves by constructing an impedance-matched surface with hybrid resonant frequencies. In their design, the spatial dimensions of each unit cell of the metasurface were deep-subwavelength scale and the unit cell thickness was smaller than the wavelength at peak absorption by two orders of magnitude. In addition to zero reflection, it was also shown that by incorporating an electromagnetic field generator in the unit cell design a 23% acoustic-electrical energy conversion efficiency could be achieved. The dispersion relations for acoustic and EM waves in a locally resonant metasurface with inclusions on the surface of an elastic solid or an interface between two elastic media was analyzed by Maznev and Gusev.[15] Using the effective medium approximation, surface inclusions on an elastic half-space were shown to induce Love-type acoustic surface waves with frequencies below the resonant frequency of the inclusions. Furthermore, the acoustic dispersion relation was shown to be analogous for EM waves guided by Lorentz oscillators acting as an interface to separate two materials with equal dielectric constants. Lamb waves travelling in an elastic meta-layer with different combinations of positive or negative effective material parameters were analyzed by Shu *et al.*[16] where the influence of the frequency dependent effective properties to the dispersion of propagating Lamb waves were examined. It was shown that for simultaneously imaginary P- and S-wave velocities in the meta-layer, the effective modulus ratio directly determined if a special propagating wave mode would be exhibited as a guided surface wave along the interface boundaries of the meta-layer. Fang *et al.*[17] presented the analytical, numerical, and experimental results on the transmission of acoustic waves through a porous metasurface with a periodically arranged microstructure consisting of four different materials. The design allowed the formation of a uniform phase shift and was capable of refracting incident acoustic waves in a controllable manner. Moreover, it was found that the propagation directions as well as the number of refracted waves were only influenced by the period lengths at specific frequencies and that the profile of the phase shift impacted the energy distribution of the refracted waves. An elastic ring-type metasurface design was proposed by Liu *et al.*[18] for cloaking a flexural Lamb wave point source by shifting, splitting, or adding angular momentum to the source signal. Lee and Kim[19] addressed a key weakness of the previously proposed elastic wave cloak designs by overcoming the inherent structural weakening traditional embedded designs by proposing an add-on plate cloak that could be retrofitted to an existing structure. The unidirectional annular metamaterial plate cloak was designed through conformal mapping and experimentally demonstrated the ability to mask holes in a thin-plate from incident elastic Lamb waves. Colombi *et al.*[20] explored the topic of tailored rainbow trapping to enhance the sensing capabilities of Rayleigh waves in an elastic metasurface. By taking advantage of the stop-band frequencies of surface waves, the rainbow trapping of elastic Rayleigh waves was experimentally demonstrated. Furthermore, the selective conversion of Rayleigh surface waves to shear waves was also demonstrated. While the ultrasonic frequency regime considered in their work (400–600 kHz) is well beyond what is what is considered here, this phenomenon can be translated to other scales as a general property of elastic waves. The enhancement of subwavelength imaging for sub- and low-ultrasonic elastic wave frequencies was examined by Lee *et al.*[21] by constructing and experimentally analyzing a hyperbolic metamaterial with a locally resonant microstructural design. Total transmission was achieved by designing the single-phase hyperbolic metamaterial lens with an extreme effective stiffness, which compensated the low effective density along the vertical direction of the lens. While the metamaterial microstructure exhibited a negative effective mass for waves propagating along the horizontal direction, the extreme effective stiffness in the vertical direction allowed for an impedance match with the base structure. Thin acrylic plates arranged in parallel and separated by small gaps were experimentally shown by Zhang *et al.*[22] to allow for the filtering of SV waves propagating in metals. It was found that the frequency range of the narrow passband filter could be easily shifted or tuned by changing the geometry of the acrylic plates that separated the two solid metal bodies. Li *et al.*[23] proposed a linear diatomic elastic metamaterial structure capable of unidirectional and asymmetric transmission of sub-ultrasonic elastic waves in multiple low frequency regions. Using analytical lattice and numerical continuum models, it was theoretically demonstrated that the dual-resonator microstructural design was capable of exhibiting broadband asymmetric transmission bands. A gradient index device was proposed by Jin *et al.*[24] for controlling the elastic waves propagating in plates. The graded phononic crystals with thickness variations demonstrated the ability to control three fundamental modes by designing three independent refractive indexes allowing for simultaneous control. Chen *et al.*[25] proposed an active gradient index metamaterial beam that was capable of being actively tuned without the need for physical microstructural modification. By using shunting circuitry with traditional piezoelectric sensors, the gradient index metamaterial beam was experimentally shown to increase both the quantity and quality of flexural wave measurement data with more than two orders of magnitude amplification and overcoming the detection limit.

To the best of the authors' knowledge, all of the previously discussed metasurface studies were focused on acoustic waves, without considering the transverse shear waves. In view of this, the main aim of this work focuses on proposing an elastic phase-controlling meta-layer by implementing the generalized Snell's law. Furthermore, it is analytically and numerically demonstrated that for a longitudinal wave with normal incidence, the propagation characteristics of the longitudinal wave and in-plane transverse wave can be manipulated by the meta-layer inclusion. It is also noted that unlike the isolation effect of negative index elastic metamaterials, this type of elastic phase-controlling meta-layer can serve as an energy absorption mechanism in structures.

II. GENERALIZED SNELL'S LAW

When the primary research focus on the metamaterials shifted from negative physical properties to controllable and frequency-dependent properties, researchers realized it was possible to manipulate a wave phase by controlling only the positive material properties of metamaterials. Based on this

idea, Yu *et al.*[26] proposed the generalized Snell's law of transmission and reflection as illustrated in Fig. 1(b).

In Fig. 1(a), a wave propagates from point O to O' with the angles of the incident and transmitted waves denoted by θ_i and θ_t, respectively. If the red and blue lines in the figure are assumed to be infinitesimally close to the wave's actual path, then the phase offset between them should be equal to zero. To calculate the phase difference of these two paths, the phase difference between $\overline{OA}$ and $\overline{OB}$, $\overline{AO'}$ and $\overline{BO'}$ can be obtained separately as

$$k_i \sin(\theta_i) dx - k_t \sin(\theta_t) dx = 0, \tag{1}$$

where dx is the distance between point A and B; $k_i = \frac{2\pi}{\lambda_i}$ and $k_t = \frac{2\pi}{\lambda_t}$ are wave numbers of the incident and transmitted wave; and λ_i and λ_t are wavelengths of the incident and transmitted wave. Rewriting Eq. (1), the Snell's law of wave transmission can be readily obtained as

$$k_i \sin(\theta_i) = k_t \sin(\theta_t). \tag{2}$$

If a meta-layer region is included to separate the incident and transmitted domains, an additional phase gradient must be considered along the x-direction of the system as shown in Fig. 1(b). Without loss of generality, we assume that the extra phase added at point A is $\emptyset$ and at B is $\emptyset + d\emptyset$. Then, Eq. (1) can be rewritten as

$$\left[k_i \sin(\theta_i) dx + (\emptyset + d\emptyset)\right] - \left[k_t \sin(\theta_t) dx + \emptyset\right] = 0. \tag{3}$$

Based on Eq. (3), we can obtain the generalized Snell's law of wave transmission as expressed in Eq. (4a) as well as the reflection relationship in Eq. (4b), where θ_r and k_r are the reflection angle and reflection wave number, respectively,

$$k_t \sin(\theta_t) = k_i \sin(\theta_i) + \frac{d\emptyset}{dx}, \tag{4a}$$

$$k_r \sin(\theta_r) = k_i \sin(\theta_i) + \frac{d\emptyset}{dx}. \tag{4b}$$

Equation (4) indicates that even if the angle of incidence is normal to the metasurface interface, the angle of transmission still can be controlled by the variable gradient phase. Based on this observation, the proposed phase-controlling elastic meta-layer is investigated in Sections III B and IV B.

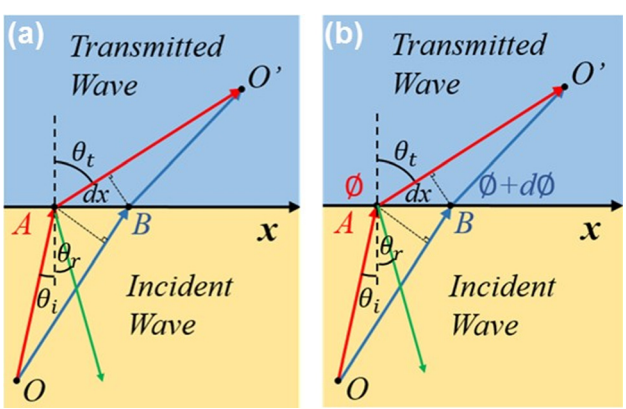

FIG. 1. Principles of (a) Snell's law and (b) the generalized Snell's law of wave transmission (Ref. 26).

III. *P*-WAVE TRANSMISSION FROM ELASTIC PHASE-CONTROLLING META-LAYER TO CONVENTIONAL MEDIUM

Unlike locally resonant elastic metamaterials, which only generate narrow band gaps, the meta-layer proposed in this work controls the maximum allowable frequency of propagating waves based on the periodic supercell's length, d, as the maximum allowable wavelength. The fundamental concept is to generate an additional phase gradient when elastic waves propagate through this meta-layer. This requires each point on the surface of the meta-layer to have its own wave propagation path without interacting with points on other paths. To meet this requirement, the meta-layer is divided into separate sections (shown as different blue color shades in Fig. 2) to avoid the elastic deformation interactions between adjacent sections. Furthermore, to generate the extra phase gradient, the materials in different sections should have the same elastic impedance but different wave velocities. In light of this, the thickness of the meta-layer significantly influences the ability to generate a different wave phase difference. With the inherent characteristic of frequency dependent properties, it has been demonstrated that elastic metamaterials can generate extreme effective Young's modulus and mass density, meaning the thickness of the meta-layer can be subwavelength scale (Ref. 27).

It should be mentioned that unlike the metasurface in the electromagnetic field, the elastic phase-controlling meta-layer is an interface with a defined thickness. Based on the design shown in Fig. 2, the transmission angle for a longitudinal wave (P-wave) can be obtained from Eq. (4). However, the displacement amplitude of the transmitted wave cannot be obtained using this approach. This is because the continuity condition at the interface between the meta-layer and conventional medium cannot be satisfied since the incident wave expression is changed by the separate section design. Therefore, instead of considering the interface between the conventional medium and the meta-layer region in the analysis, a surface of close proximity is considered in Sec. III A.

A. Wave form derivation

Figure 3 shows the elastic wave propagation from the phase-controlling meta-layer to the conventional medium for

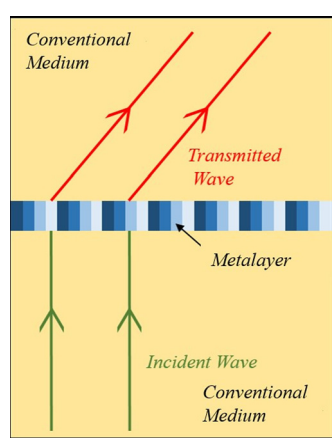

FIG. 2. Sketch of wave propagation through a meta-layer interface.

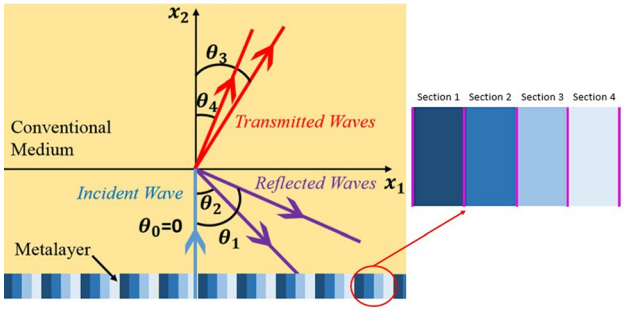

FIG. 3. Elastic wave fields from meta-layer to conventional medium.

a longitudinal wave with an incident angle of zero. To avoid the mutual interference of the elastic deformation in each section (e.g., Secs. I and II in Fig. 3), the interfaces between adjacent sections in the meta-layer (cyan lines in Fig. 3) are designed to be fixed in the x_1 direction. Due to this constrained interface feature, the continuity condition is not satisfied at the interface between the meta-layer and the conventional medium. To derive the wave form of the transmitted waves, the surface (surface $x_2 = 0$ shown in Fig. 3) close to the meta-layer and the conventional medium interface is considered instead. Since the surface $x_2 = 0$ is close to the meta-layer/conventional medium interface, the interaction between waves propagating through different meta-layer sections can be ignored below the surface $x_2 = 0$.

When a plane longitudinal wave with normal incidence impinges on the meta-layer interface, two types of transmitted waves (P- and SV-wave) are generated.[28] Similarly, P- and SV-waves will also be reflected back into the conventional background medium from the meta-layer interface. For a harmonic waveform, the displacements of the transmitted and reflected waves are given by

$$\vec{u}^{(n)} = A_n \vec{d}^{(n)} \exp(i\eta_n), \tag{5}$$

where $n = 1, 2, 3$, or 4 denote the reflected P-wave, reflected SV-wave, transmitted P-wave, and transmitted SV-wave, respectively, and A_n is the amplitude of each wave.[28] The travel direction of a particle is denoted by $\vec{d}^{(n)}$, and the wave propagation phase can be expressed as $\eta_n = k_n(x_1 p_1{}^{(n)} + x_2 p_2{}^{(n)} - C_n t)$, where p_j ($j = 1, 2$) is the wave propagation direction and C_n is the wave speed.

With respect to Eq. (5), the incident wave expression is changed by the meta-layer component, which can now be expressed as

$$u_1{}^{(0)} = A_0 \exp\left(i x_1 \frac{d\emptyset}{dx}\right) \sin(\theta_0) * \exp[i k_0 (x_1 \sin(\theta_0) + x_2 \cos(\theta_0) - C_0 t)], \tag{6a}$$

$$u_2{}^{(0)} = A_0 \exp\left(i x_1 \frac{d\emptyset}{dx}\right) \cos(\theta_0) * \exp\left[i k_0 \left(x_1 \sin(\theta_0) + x_1 \frac{d\emptyset}{dx} + x_2 \cos(\theta_0) - C_0 t\right)\right]. \tag{6b}$$

At the interface ($x_2 = 0$), the perfect contact assumption requires the displacements and stresses to be continuous, i.e.,

$$u_j{}^{(0)} + u_j{}^{(1)} + u_j{}^{(2)} = u_j{}^{(3)} + u_j{}^{(4)}, \tag{7a}$$

$$\tau_{2j}{}^{(0)} + \tau_{2j}{}^{(1)} + \tau_{2j}{}^{(2)} = \tau_{2j}{}^{(3)} + \tau_{2j}{}^{(4)}, \tag{7b}$$

where $j = 1, 2$. Equation (7) must be valid for all values of x_1 and t, which implies

$$k_0 \sin(\theta_0) + \frac{d\emptyset}{dx} = k_1 \sin(\theta_1) = k_2 \sin(\theta_2) = k_3 \sin(\theta_3) = k_4 \sin(\theta_4), \tag{8a}$$

$$k_0 C_0 = k_1 C_1 = k_2 C_2 = k_3 C_3 = k_4 C_4. \tag{8b}$$

It is obvious that Eq. (8a) is the same expression of the generalized Snell's law shown in Eq. (4). By substituting Eqs. (5), (6), and (8) into Eq. (7), the wave amplitude relations can be obtained as

$$\begin{bmatrix} -\sin(\theta_1) & -\cos(\theta_2) & \sin(\theta_3) & -\cos(\theta_4) \\ \cos(\theta_1) & -\sin(\theta_2) & \cos(\theta_3) & \sin(\theta_4) \\ \sin(2\theta_1) & \kappa\cos(2\theta_2) & \sin(2\theta_3) & -\kappa\cos(2\theta_4) \\ -\lambda - 2\mu\cos^2(\theta_1) & \kappa\mu\sin(2\theta_2) & \lambda + 2\mu\cos^2(\theta_3) & \kappa\mu\sin(2\theta_4) \end{bmatrix} \begin{bmatrix} A_1 \\ A_2 \\ A_3 \\ A_4 \end{bmatrix} = A_0 \begin{bmatrix} \sin(\theta_0) \\ \cos(\theta_0) \\ \sin(2\theta_0) + \cos(\theta_0) \dfrac{d\emptyset}{k_0 dx} \\ \lambda + 2\mu\cos^2(\theta_0) + \lambda\sin(\theta_0) \dfrac{d\emptyset}{k_0 dx} \end{bmatrix}, \tag{9}$$

where λ and μ are Lamé constants, and κ is ratio of P-wave velocity to SV-wave velocity.

Solving Eq. (9) and substituting the results into Eq. (5), the final harmonic wave form of the transmitted and reflected waves can be readily obtained.

B. Transmitted wave manipulation

Based on the previous analytical derivation, the manipulation of the transmitted waves with the elastic phase-controlling meta-layer will now be illustrated. In Table I, the material properties, angle of incidence, frequency, and wave lengths of the P-(λ_L) and SV-waves (λ_T) are listed. Also listed in Table I is the phase gradient (d in meters), which is the periodic length of the meta-layer element. It should be noted that the effect of meta-layers is caused by the introduction of an additional phase gradient rather than the change of the conventional material properties listed in Table I.

TABLE I. Material properties and wave constants for each case.

	Young's modulus, E (MPa)	Density, ρ (kg/m^3)	Poisson's ratio, υ	Incident angle θ_i (°)	Frequency, f (Hz)	Longitudinal wavelength, λ_L (m)	Transverse wavelength, λ_T (m)	Gradient phase, $\frac{d\varnothing}{dx} = \frac{2\pi}{d}$
Case 1	1	1	0	0	10	10	7.071	$2\pi/6$
Case 2	1	1	0	0	10	10	7.071	$2\pi/12$
Case 3	1	1	0	0	10	10	7.071	$2\pi/9$
Case 4	1	1	0	0	10	10	7.071	$-2\pi/9$
Case 5	1	1	0	20	10	10	7.071	$2\pi/9$
Case 6	1	1	0	−20	10	10	7.071	$2\pi/9$
Case 7	70×10^5	2.7×10^3	0.33	0	100	61.98	31.22	$2\pi/4$
Case 8	70×10^5	2.7×10^3	0.33	0	1000	6.198	3.122	$2\pi/4$

For case 1, the chosen periodic length of $d = 6\,\mathrm{m}$ is smaller than the wavelengths of the P- and SV-waves. In Fig. 4, the displacement components in the horizontal and vertical directions are given by x_1 and x_2, respectively, and $x_2 = 0$ is assumed to be the surface located infinitely close to the interface between the meta-layer and conventional medium. It is obvious from the figure that if either wavelengths, λ_L or λ_T, are larger than the periodic length d, there will be zero incident wave transmission. Compared with the critical angle predicted by Eq. (4a)

$$k_t \sin(\theta_t) = k_i \sin(\theta_i) + \frac{d\emptyset}{dx} = \frac{2\pi}{d} \rightarrow \sin(\theta_t) = \frac{2\pi}{d * k_t} = \frac{2\pi}{d} * \frac{\lambda_t}{2\pi} = \frac{\lambda_t}{d}, \tag{10}$$

it is clear that the previously derived Eq. (9) has a good agreement with the generalized Snell's law.

For case 2 in Table I, the periodic length d is increased to a larger value than the wave lengths of the P- and SV-waves. Figure 5 shows the displacement fields for the P- and SV-waves in the x_1 and x_2 directions where it is clear that waves can easily propagate through the meta-layer when the wave length, λ_L or λ_T, is larger than the periodic length of the meta-layer, d. The abnormal wave form shown in Fig. 5 is caused by the combination of P- and SV-wave transmission fields.

In cases 3 and 4, the same phase gradient is considered in the meta-layer region but opposite in sign. The periodic length d of these two cases is smaller than the wave length of the P-wave but larger than that of the SV-wave. Figures 6 and 7 show the displacements u_1 and u_2 for cases 3 and 4, respectively. Since the periodic length d is larger than the shear wave length, λ_T, but smaller than the plane wave length, λ_L, only SV-waves can propagate through the meta-layer region and with a transmission angle of 51.78°, which is in agreement with that obtained from Eq. (10). Furthermore, the perfect harmonic waveform is shown in the transmission domain in both figures. Comparing Figs. 6 and 7, it is apparent that without changing the angle of incidence, the negative phase gradient induces a negative transmission angle, and thus, enlarges the controllable angle of transmitted waves.

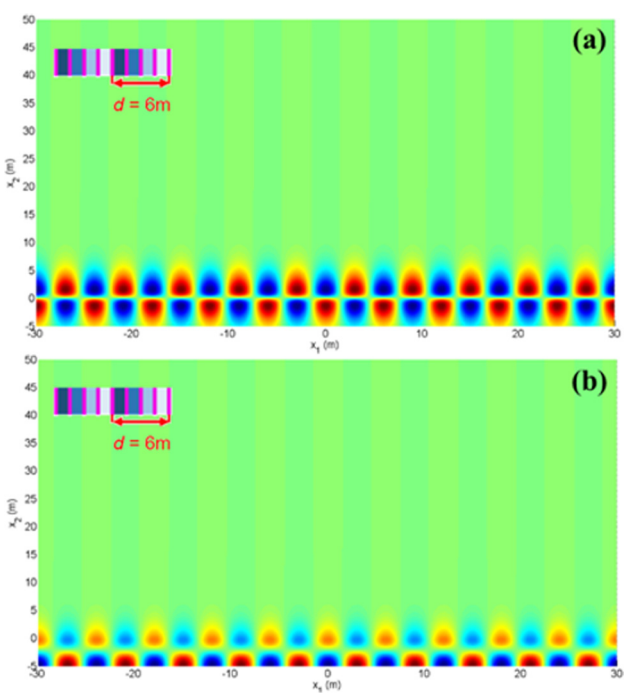

FIG. 4. (a) Displacement u_1 for case 1 ($d < \lambda_T$ and $d < \lambda_L$) and (b) displacement u_2 for case 1 ($d < \lambda_T$ and $d < \lambda_L$).

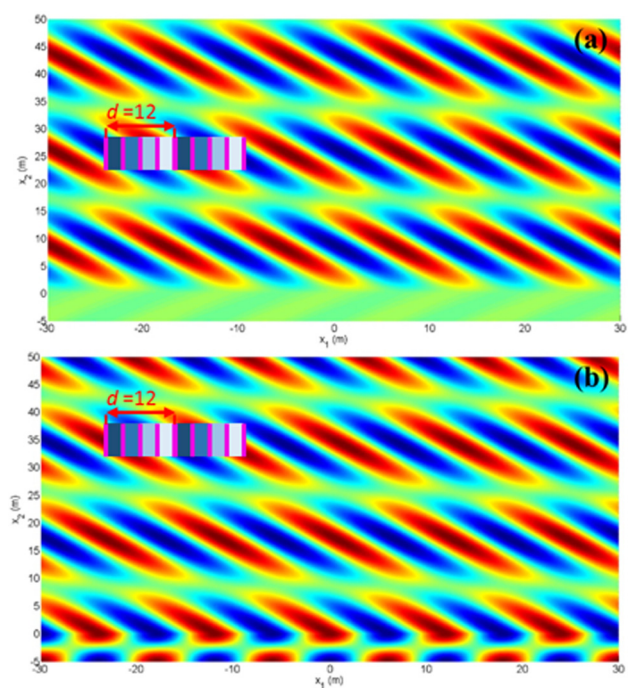

FIG. 5. (a) Displacement u_1 for case 2 ($d > \lambda_T$ and $d > \lambda_L$) and (b) displacement u_2 for case 2 ($d > \lambda_T$ and $d > \lambda_L$).

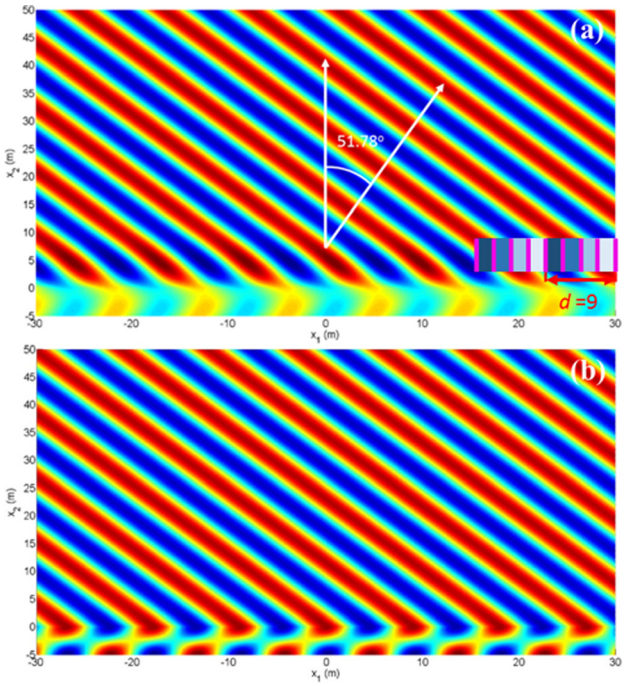

FIG. 6. (a) Displacement u_1 for case 3 ($d > \lambda_T$ and $d < \lambda_L$) and (b) displacement u_2 for case 3 ($d > \lambda_T$ and $d < \lambda_L$).

In cases 5 and 6, the same phase gradient is used with incident wave angles of opposite sign. Figures 8 and 9 show the displacements u_1 and u_2 for cases 5 and 6, respectively. It is clear that for case 5, with a positive incident angle, no wave propagates through the meta-layer. However, for case 6 with a negative angle of incidence, both *P*-wave and *SV*-waves can propagate through the meta-layer. This non-symmetric phenomenon can be easily derived from Eq. (8a).

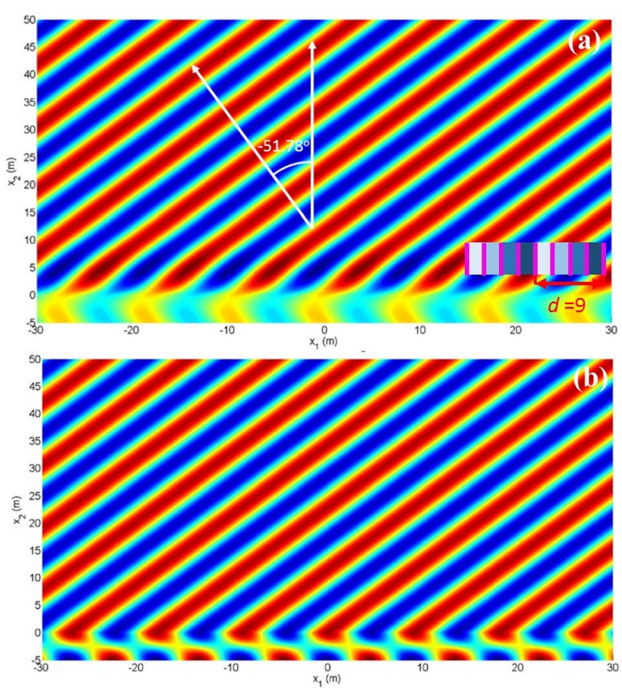

FIG. 7. (a) Displacement u_1 for case 4 ($d > \lambda_T$ and $d < \lambda_L$) and (b) displacement u_2 for case 4 ($d > \lambda_T$ and $d < \lambda_L$).

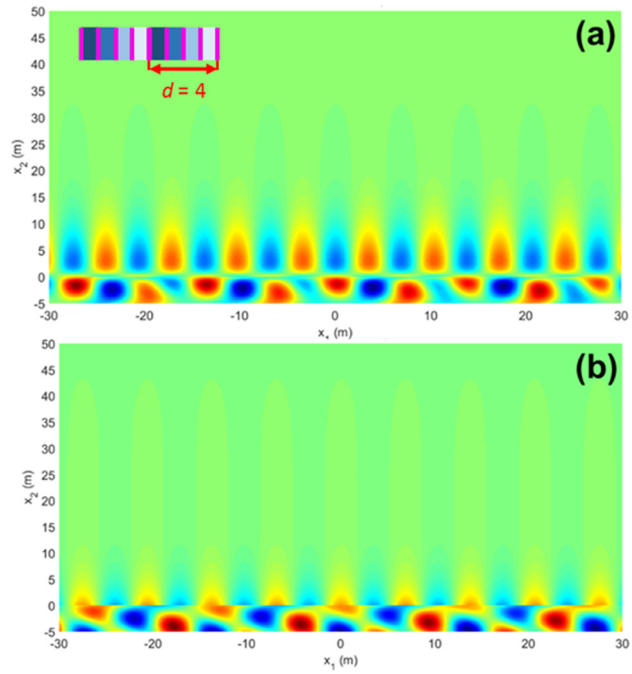

FIG. 8. Case 5 displacement for (a) u_1 and (b) u_2.

In the last two cases, the real material properties of aluminum are considered. Figures 10 and 11 show the displacements u_1 and u_2 for case 7 and case 8, respectively. Using the realistic material properties, it can be seen that the same phenomenon is exhibited and thus validates the proposed meta-layer concept for the potential real-world engineering applications.

It should be noted that the longitudinal wave is always larger than the transverse wave in isotropic materials. Thus, to obtain a pure *SV*-wave the largest periodic length d is limited by the longitudinal wave length, λ_L. In other words, the

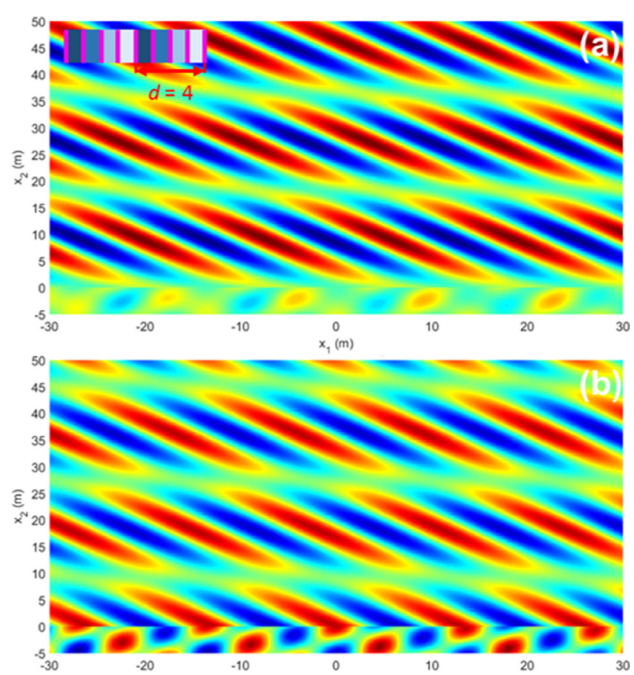

FIG. 9. Case 6 displacement for (a) u_1 and (b) u_2.

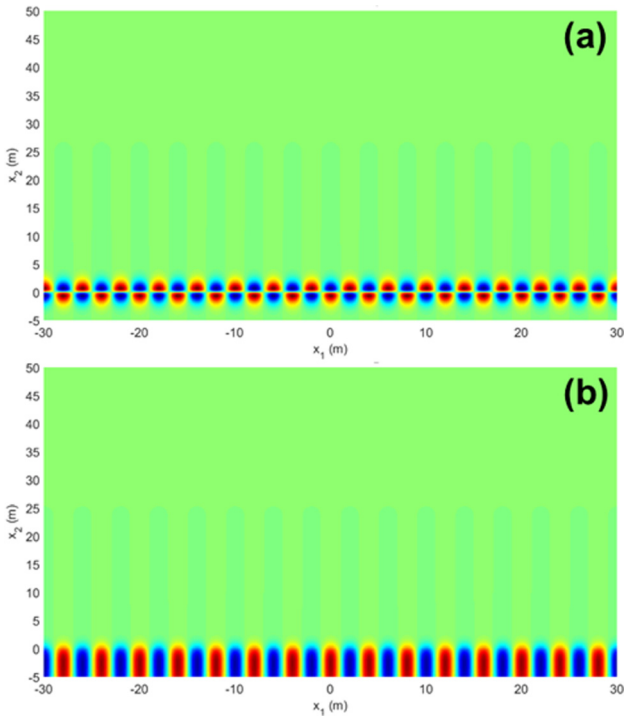

FIG. 10. Case 7 displacement for (a) u_1 and (b) u_2 ($d < \lambda_T$ and $d < \lambda_L$).

minimum *SV*-wave transmission angle is limited by the longitudinal wavelength. For isotropic materials, λ_L changes with the Poisson's ratio as $\lambda_L = \frac{1}{f} * \sqrt{\frac{E(1-\nu)}{\rho(1+\nu)(1-2\nu)}}$, where E, ρ, and ν are Young's modulus, density, and Poisson's ratio of a certain material. Figure 12 shows the relationship between the minimum *SV*-wave transmission angle and the Poisson's ratio. The figure indicates that the minimum *SV* transmission angle decreases when the Poisson's ratio

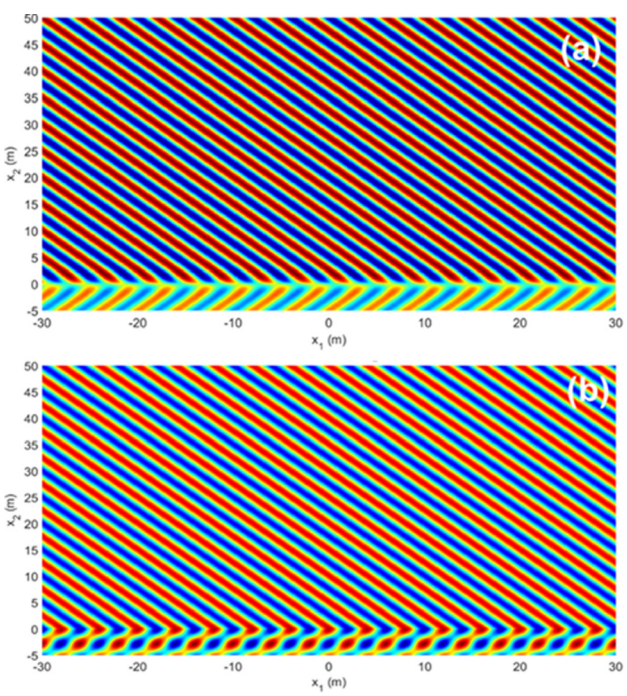

FIG. 11. Case 8 displacement for (a) u_1 and (b) u_2 ($d > \lambda_T$ and $d < \lambda_L$).

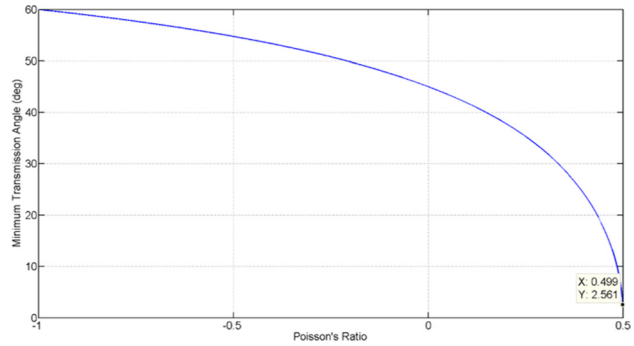

FIG. 12. Minimum *SV* transmission angle vs. Poisson's ratio ($d > \lambda_T$ and $d < \lambda_L$).

increases, and when the Poisson's ratio approaches 0.5, the transmission angle is close to 0°. In other words, by controlling the gradient phase, the transmitted wave can be switched to a chosen direction.

C. Time-average stress power

To quantify the transmitted wave energy, the average power $\langle P \rangle$ is calculated, which represents the average energy transmission per unit time and per unit area.[28] The average longitudinal wave power, $\langle P_L \rangle$, and average transverse wave power, $\langle P_T \rangle$, can be expressed as

$$\langle P_L \rangle = \frac{1}{2}(\lambda + 2\mu)\frac{\omega^2}{c_L}A^2, \tag{11a}$$

$$\langle P_T \rangle = \frac{1}{2}\mu\frac{\omega^2}{c_T}A^2. \tag{11b}$$

In Eq. (11), λ and μ are Lamé constants. Based on Eq. (9), Table II lists the transmitted wave amplitudes and the corresponding average power for the first four cases listed in Table I. The extremely small average power in Table II indicates that no corresponding wave can propagate through the meta-layer. This is the case for longitudinal waves in cases 1, 3, and 4 and transverse waves in case 1. This is also in good agreement with the previously stated conclusion that if the periodic length d is smaller than the incident longitudinal wave length or transverse wave length, the corresponding wave cannot propagate through the meta-layer region.

IV. NUMERICAL SIMULATION OF WAVE PROPAGATING THROUGH PHASE-CONTROLLING META-LAYER

A. Design of elastic phase-controlling meta-layer

Generally, there are two methods to realize a phase-controlling meta-layer by implementing the fundamental

TABLE II. Transmitted wave amplitude and average power of each case in Table I.

	A_3	$\langle P_L \rangle$	A_4	$\langle P_T \rangle$
Case 1	0.5	5.04×10^{-10}	0.5893	3.50×10^{-10}
Case 2	1.0905	1.30×10^{7}	0.8103	7.41×10^{6}
Case 3	0.5	3.36×10^{-10}	1.2909	1.44×10^{7}
Case 4	0.5	3.36×10^{-10}	−1.2909	1.44×10^{7}

TABLE III. Material properties and wave constants for FEM model.

	Effective Young's modulus, E_{eff} (MPa)	Density, ρ (kg/m^3)	Poisson's ratio, υ	Frequency, f (Hz)	Longitudinal wave velocity, C_L(m/s)
Conventional material	1	0.1	0	10	100
Elastic metamaterial	0.166	0.6	0	10	16.666

metamaterial concept. The first is to use the elastic metamaterials with different local resonators in each meta-layer section; the second is to use the same elastic metamaterial but with different thicknesses in each meta-layer section. To simplify the potential real-world applications, the second method is adopted in this section. The discrete elastic phase-controlling meta-layer model shown in Fig. 13 is adopted to replace the continuum phase gradient meta-layer model. For each periodic meta-layer element shown in Fig. 13, the white areas denote an elastic metamaterial while the green areas represent a conventional material. Since the phase velocities of the elastic metamaterial and the conventional material are different, in the periodic element shown in Fig. 13, the meta-layer will generate an extra phase difference from 0 to 2π at its two surfaces. With the same periodic length d, a four-section design [Fig. 13(a)] and a ten-section design [Fig. 13(b)] are compared in this section. Setting periodic conditions at the left and right boundaries, the semi-infinite problem is simplified to the one period length meta-layer shown in Fig. 13. To maintain the incident wave in longitudinal wave form through meta-layer, the interface between two adjacent sections in the meta-layer (red lines in Fig. 13) is assumed to be a crack with symmetric boundary conditions in the lateral direction.

In addition, the uniform phase gradient requires a constant phase difference between each adjacent meta-layer section. Therefore, the mechanical impedance of the elastic metamaterial and the conventional material should be matched, with the thickness of the metamaterial in each section calculated as

$$l_i = \frac{\emptyset_i}{\omega}\frac{C_L{}^0 C_L{}^1}{C_L{}^0 - C_L{}^1} = \frac{2i}{n}, \ (\mathrm{i} = 1, 2, \ldots, \mathrm{n}-1), \qquad (12)$$

where n is the periodic section number, $\emptyset_i$ is the extra phase generated by each meta-layer section, and $C_L{}^0$ and $C_L{}^1$ are the longitudinal wave speeds in the conventional material and elastic metamaterial, respectively. Corresponding to the material properties listed in Table I, the specific case shown in Table III is considered where the metamaterial thickness in each section is obtained from Eq. (12). The purpose of the following numerical simulation is to verify the meta-layer properties demonstrated earlier, including the frequency threshold of waves propagating from the meta-layer, and a certain frequency range to convert longitudinal wave into transverse wave.

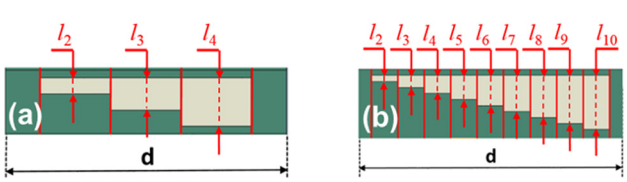

FIG. 13. Discrete phase-controlling meta-layer periodic element model: (a) four-section design and (b) ten-section design.

B. Numerical simulation results and discussion

To verify the analytical solutions in Sec. III, the numerical simulations of the longitudinal wave propagation through the meta-layer with different periodic lengths are performed using the finite element code ABAQUS Explicit. To generate the incident longitudinal wave, a harmonic displacement boundary condition is considered while the periodic boundary conditions are defined on the two edges perpendicular to the wave propagation direction.

Corresponding to case 1 in Table I where the periodic length d (= 6) is smaller than the transverse wave length λ_T, Fig. 14 compares the wave propagation within the four- and ten-section designs. From Figs. 14(c) and 14(d), it is clear that the wave cannot propagate through the meta-layer region. While this agrees with the analytical solution, in Fig. 14(b) it seems that the wave can indeed propagate through the meta-layer interface. This phenomenon is caused by the

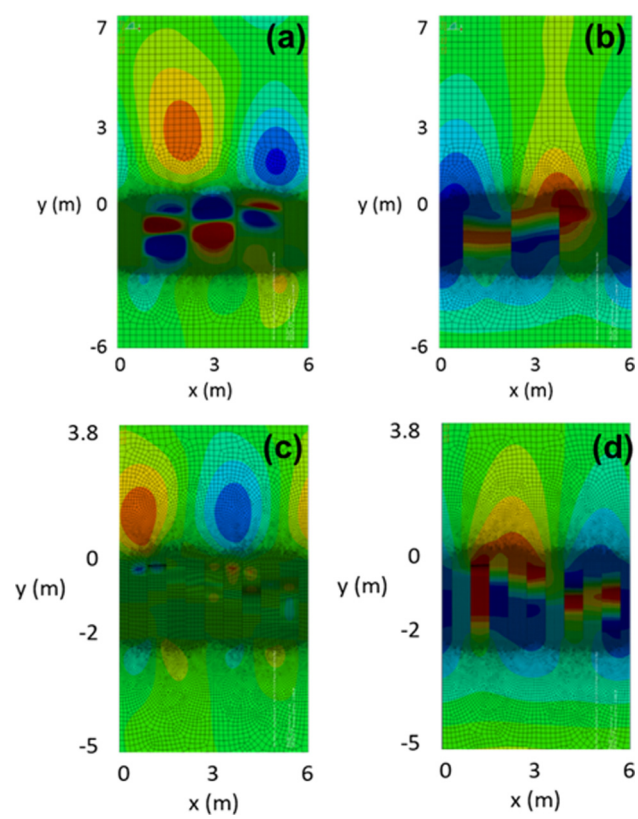

FIG. 14. Snapshot of displacement fields u_1 and u_2 in four- and ten-section designs with a periodic meta-layer element length of $d = 6$ m ($d < \lambda_T$ and $d < \lambda_L$): (a) displacement u_1 of four-section design, (b) displacement u_2 of four-section design, (c) displacement u_1 of ten-section design, and (d) displacement u_2 of ten-section design.

non-uniform phase gradient, and thus, to fabricate a more accurate elastic phase-control meta-layer, more sections need to be implemented.

In addition, to obtain the proximate position of the interaction interface considered in Sec. III A, Fig. 15 shows the displacement amplitude u_1 of points at different distances away from the meta-layer surface. Since the incident wave does not have a u_1 component, the continuity condition on the interaction surface requires the displacement amplitude u_1 be equal to zero. Therefore, the proximate position of interaction interface should be close to 0.0629 m for this case.

For case 2 where the periodic length of $d = 12$ m is larger than the longitudinal wave length λ_L, the wave propagation for the four- and ten-section designs are shown in Fig. 16. It is clear from the figures that the wave can propagate through the meta-layer, and the wave form shown in Figs. 16(c) and 16(d) are in agreement with those shown in Figs. 5(a) and 5(b). Comparing Figs. 16(a) and 16(b) with Figs. 16(c) and 16(d), it is obvious that the imperfect wave form is caused by the non-uniform phase gradient in the meta-layer region, and the ten-section design can generate a relatively uniform phase gradient to accurately realize the meta-layer concept.

In case 3 and case 4 for which the periodic length d (=9 m) is larger than the transverse wave length λ_T, but smaller than the longitudinal wave length λ_L, only the *SV*-wave can propagate through the meta-layer interface. The designs for a ten-section design with positive and negative phase gradients are shown in Figs. 17(a) and 17(b), respectively.

Since the *SV*-waves propagation direction cannot be obtained directly from the movement of the nodes, three points are selected to calculate the propagation direction as shown in Fig. 18. In the area above the meta-layer, the points P_1 and P_2 coincide on the same vertical line while P_1 and P_3 are aligned horizontally. The distance between points P_2 and P_1 is denoted by Δy, and the distance between points P_3 and P_1 is Δx. Using this approach, the angle between the *SV*-wave propagation direction and the x-axis (transmission angle) denoted by, α, can be obtained as

$$\cos(\alpha) = \frac{C_T \Delta t_x}{\Delta x}, \tag{13a}$$

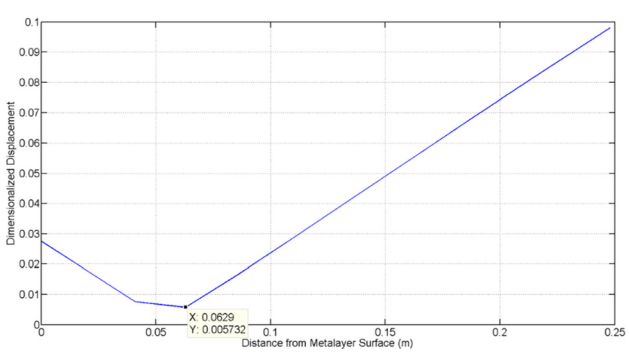

FIG. 15. Displacement u_1 amplitude at different distances from meta-layer surface.

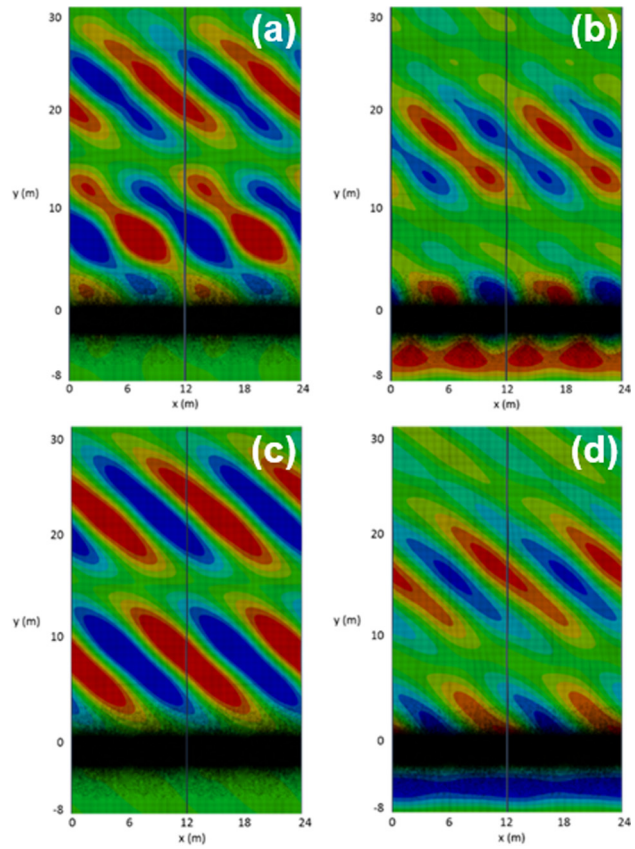

FIG. 16. Snapshot of displacement fields u_1 and u_2 in four- and ten-section designs with a periodic meta-layer element length of $d = 12$ m ($d > \lambda_T$ and $d > \lambda_L$): (a) Displacement u_1 of four-section design, (b) Displacement u_2 of four-section design, (c) displacement field u_1 of ten-section design, and (d) displacement u_2 of ten-section design.

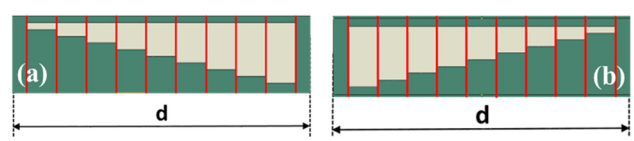

FIG. 17. Discrete meta-layer models for (a) ten-section (positive phase gradient) and (b) ten-section (negative phase gradient).

$$\sin(\alpha) = \frac{C_T \Delta t_y}{\Delta y}, \tag{13b}$$

where Δt_x and Δt_y are the times of the same wave peak propagating from P_1 to P_3 and P_1 to P_2, respectively.

Figure 19 shows the displacement amplitudes at the three points selected on the ten-section design model. The

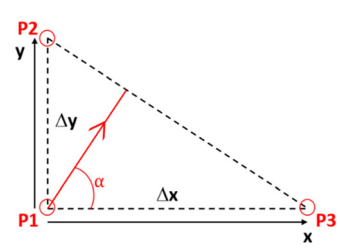

FIG. 18. Three points selected to calculate the transmitted wave propagation direction.

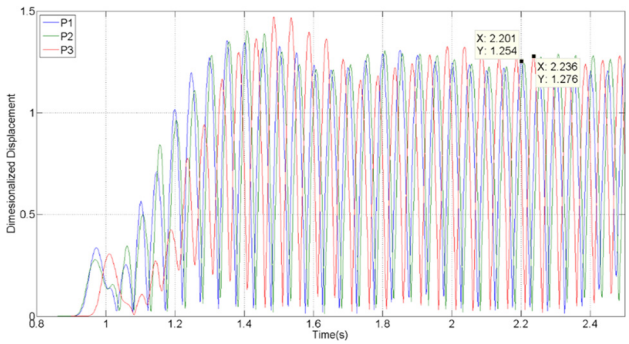

FIG. 19. Displacement amplitudes history of three points selected on the ten-section design model.

distance between points P_1 and P_2 is 4, and $\Delta t_x = 0.035$ s. Based on Eq. (13a), the wave propagation direction calculated as $+51.7°$, which is very close to the analytical solution (51.8°) obtained by the generalized Snell's law in Eq. (4). It is also noted that the transmitted waves normalized amplitude is around 1.27, which is extremely close to the analytical solution (1.29) obtained in Table II.

Figure 20 illustrates the wave propagation characteristics in the ten-section meta-layer design with positive and negative phase gradients. Comparing Fig. 20 with the analytical solutions obtained in Figs. 6 and 7, it is obvious that the wave form has become imperfect. This phenomenon is caused by the imperfections present in the uniform phase gradient generated by the meta-layer. These imperfections were also addressed by Li *et al.*,[12] who concluded that these imperfections were the result of the mismatched wave amplitude along the metasurface.

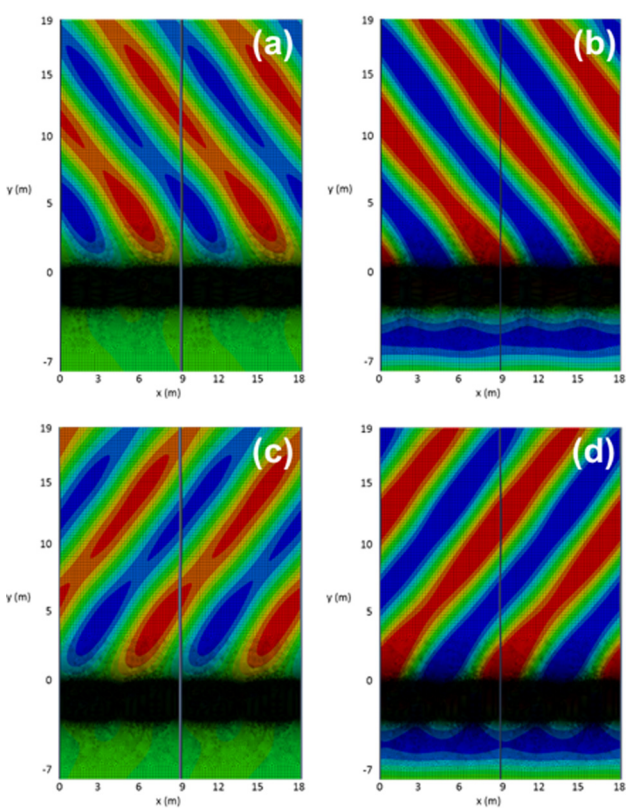

FIG. 20. Snapshot of displacement fields with periodic length of meta-layer element $d = 9$ m ($d > \lambda_T$ and $d < \lambda_L$) (a) u_1 (positive phase gradient), (b) u_2 (positive phase gradient), (c) u_1 (negative phase gradient), and (d) u_2 (negative phase gradient).

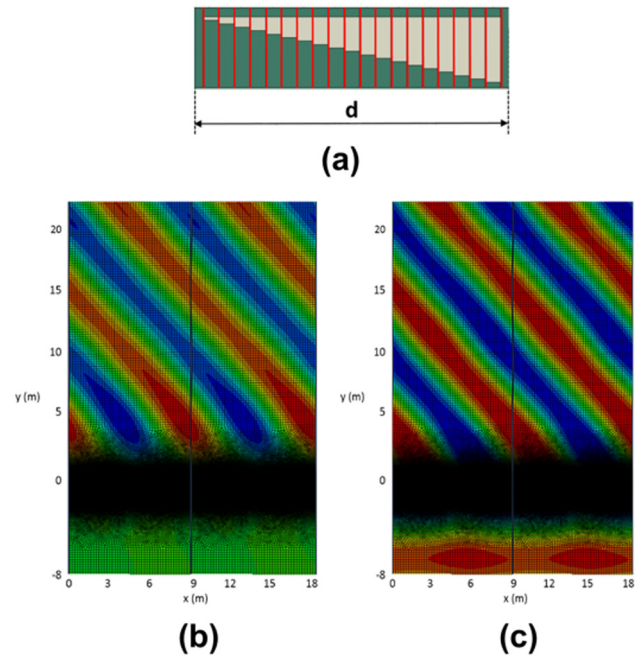

FIG. 21. (a) Discrete twenty-section meta-layer model with a periodic length of $d = 9$ m ($d > \lambda_T$ and $d < \lambda_L$) and snapshots of displacement fields (b) u_1 and (c) u_2.

To verify that the ten-section design has a sufficiently uniform gradient, using the same working conditions as Fig. 20, Fig. 21 illustrates the result of a twenty-section meta-layer

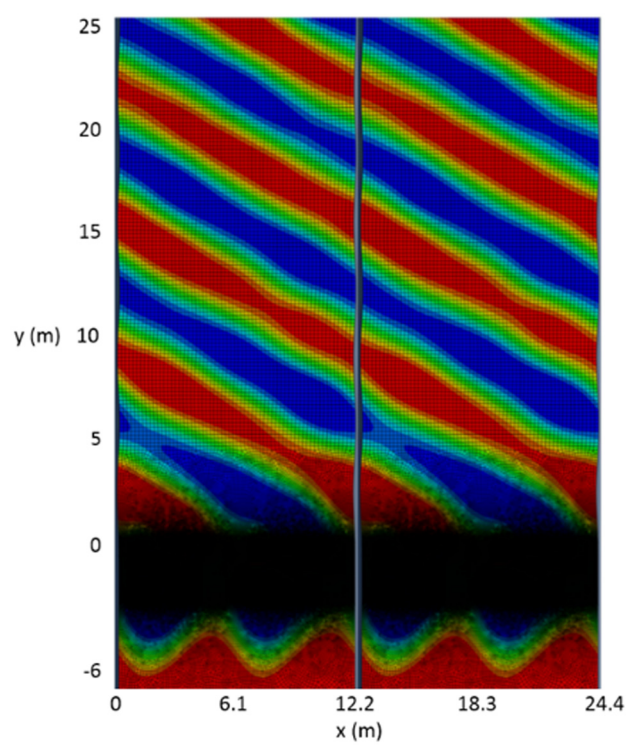

FIG. 22. Snapshot of displacement u_1 of ten-section design with periodic length $d = 12.2$ m.

design. The results are very similar to those obtained for the ten-section design, which indicates that the ten-section design is uniform enough to realize the meta-layer concept.

Finally, as discussed in the last paragraph of Sec. III B, the minimum *SV*-wave transmission angle decreases as the Poisson's ratio increases. Therefore, with a larger Poisson's ratio, the pure *SV*-wave transmission can reach a smaller transmission angle. In Fig. 22, the *SV*-wave transmission for a material with a Poisson's ratio of 0.35 is illustrated with a transmission angle of 29.9° obtained through numerical simulation.

V. CONCLUSION

In this work, we propose a gradient-phase based meta-layer design with the goal of demonstrating a low frequency threshold to effectively inhibit the propagation of elastic waves over certain frequencies while also exhibiting longitudinal to shear wave mode conversion. Unlike the narrow resonance induced band gaps exhibited by locally resonant metamaterial designs, the meta-layer design proposed in this work is dependent on the periodic supercells length, which sets the maximum wavelength of waves able to propagate through the structure. Analysis of the elastic phase-controlling meta-layer design was conducted using the generalized Snell's law. It was found that for a normally incident longitudinal wave propagating through the meta-layer interface, both longitudinal and in-plane transverse waves can be effectively manipulated. This wave manipulation property is directly related to the metamaterial thickness in each section of the meta-layer region. Furthermore, by controlling the thickness of the sections in the meta-layer, a phase gradient was realized to satisfy the generalized Snell's law. It has been demonstrated that for an incident longitudinal wave, the transmitted waves can be directly controlled with the periodic length of the meta-layer region. This means that the transmission of incident longitudinal waves through the meta-layer region is directly dependent on whether the wave length is shorter or longer than the periodic length of the meta-layer element. If the periodic length of the meta-layer element is larger than the transverse wavelength, but smaller than the longitudinal wavelength, only the shear waves can pass through the meta-layer region. This is due to the incident longitudinal wave undergoing a mode conversion and becoming a pure in-plane shear wave. In addition, by controlling the meta-layer's phase gradient and Poisson's ratio, the transmitted pure shear wave's direction can be controlled. Since the most common and damaging elastic waves are lower than 200 Hz, the concept outlined in this work has potential applications in civil, industrial, and mechanical engineering fields. Some potential applications include earthquake protection for structures through seismic shielding, high energy vibration isolation, as well as many others in the fields of dynamics.

ACKNOWLEDGMENTS

This work was supported by DTRA Grant No. DTRA1-12-1-0047 and AFOSR Grant No. FA9550-15-1-0016.

[1]V. G. Veselago, Sov. Phys. Usp. **10**, 509 (1968).
[2]A. Sihvola, Metamaterials **1**, 2 (2007).
[3]D. R. Smith, W. J. Padilla, D. C. Vier, S. C. Nemat-Nasser, and S. Shultz, Phys. Rev. Lett. **84**, 4184 (2000).
[4]J. Pendry, Phys. Rev. Lett. **76**, 4773 (1996).
[5]J. B. Pendry, A. J. Holden, D. J. Robbins, and W. J. Stewart, IEEE Trans. Microwave Theory Tech. **47**, 2075 (1999).
[6]Z. Liu, X. Zhang, Y. Mao, Y. Y. Zhu, A. Modinos, Z. Yang, C. T. Chan, and P. Sheng, Science **289**, 1734 (2000).
[7]N. Fang, D. Xi, J. Xu, M. Ambati, W. Srituravanich, C. Sun, and X. Zhang, Nat. Mater. **5**, 452 (2006).
[8]J. Mei and Y. Wu, New J. Phys. **16**, 123007 (2014).
[9]G. Ma, M. Yang, S. Xiao, Z. Yang, and P. Sheng, Nat. Mater. **13**, 873 (2014).
[10]J. Zhao, B. Li, Z. Chen, and C. W. Qiu, Sci. Rep. **3**, 2537 (2013).
[11]J. Zhao, B. Li, Z. N. Chen, and C. W. Qiu, Appl. Phys. Lett. **103**, 151604 (2013).
[12]Y. Li, B. Liang, Z. M. Gu, X. Y. Zou, and J. C. Cheng, Sci. Rep. **3**, 2546 (2013).
[13]R. Zhu, X. N. Liu, G. K. Hu, C. T. Sun, and G. L. Huang, Nat. Commun. **5**, 5510 (2014).
[14]H. Zhu and F. Semperlotti, Phys. Rev. Lett. **117**, 034302 (2016).
[15]A. A. Maznev and V. E. Gusev, Phys. Rev. B **92**, 115422 (2015).
[16]H. Shu, L. Xu, X. Shi, L. Zhao, and J. Zhu, J. Appl. Phys. **120**, 165103 (2016).
[17]Y. Fang, X. Zhang, and J. Zhou, Appl. Phys. Lett. **110**, 171904 (2017).
[18]Y. Liu, Z. Liang, F. Liu, O. Diba, A. Lamb, and J. Li, Phys. Rev. Lett. **119**, 034301 (2017).
[19]M. K. Lee and Y. Y. Kim, Sci. Rep. **6**, 20731 (2016).
[20]A. Colombi, V. Ageeva, R. J. Smith, A. Clare, R. Patel, M. Clark, D. Colquitt, P. Roux, S. Guenneau, and R. V. Craster, Sci. Rep. **7**, 6750 (2017).
[21]H. Lee, J. H. Oh, H. M. Seung, S. H. Cho, and Y. Y. Kim, Sci. Rep. **6**, 24026 (2016).
[22]J. Zhang, Y. Liu, W. Yan, and N. Hu, AIP Adv. **7**, 085318 (2017).
[23]B. Li, S. Alamri, and K. T. Tan, Sci. Rep. **7**, 6226 (2017).
[24]Y. Jin, D. Torrent, Y. Pennec, Y. Pan, and B. Djafari-Rouhani, Sci. Rep. **6**, 24437 (2016).
[25]Y. Y. Chen, R. Zhu, M. V. Barnhart, and G. L. Huang, Sci. Rep. **6**, 35048 (2016).
[26]N. Yu, P. Genevet, M. A. Kats, F. Aieta, J. P. Tetienne, F. Capasso, and A. Gaburro, Science **334**, 333 (2011).
[27]Y. Liu, X. Shen, X. Su, and C. T. Sun, J. Vib. Acoust. **138**, 21011 (2016).
[28]J. D. Achenbach, *Wave Propagation in Elastic Solids* (North-Holland Pub. Co, 1973).